Chapter 4

Using Tidal Modulation of Ice Stream Motion to Constrain Viscoelastic Parameters *in Situ*

A phase delay in the response of a body to an oscillatory load is potentially related to that body behaving as a viscoelastic material. Geodetic studies of Rutford Ice Stream, Antarctica and Helheim Glacier, Greenland definitively show there is a significant phase lag between the tidally modulated surface motion of grounded ice and the peak ocean tides. In this chapter, we present a preliminary modeling framework outlining the relationship between the rheological parameters of a viscoelastic ice stream and the expected phase delay in its response to an oscillatory forcing. We then use these one- and two-dimensional results to suggest the configuration and requirements of a geodetic survey with the specific goal of constraining the viscoelastic parameters of *in situ* glacial ice.

4.1 Introduction

The previous two chapters demonstrated that ice streams are unlikely to transmit tidal stress through the bulk of the ice stream itself to the extreme distances seen observationally. However, near to the grounding line, a tidal load can still be transmitted through the ice stream bulk. And throughout the ice stream, the issue of the observed phase delay in the ice stream's response to ocean tides remains. As ice behaves as a viscoelastic material over tidal timescales (e.g., chapter 3 of this thesis), our expectation is that the near-grounding line behavior of an ice stream could provide a measurement of the viscoelastic parameters for *in situ* ice. While such a measurement would necessarily be convolved with other processes that are tied to the ocean tides, this chapter provides a "proof-of-concept" for using observed tidal phase lags to constrain viscoelastic properties for glacial ice.

Our goal is to establish a methodology that uses the multiple timescales of the oscillatory tidal load in conjunction with the observed phase shift in tidal response to infer constraints on the ice stream's viscoelastic parameters. As most of the introductory material has already been covered in chapters 2 and 3, we address only the most salient points in this chapter's introduction, and suggest that this chapter is best understood after reading the introductory material in these two earlier chapters.

High-rate continuous global positioning satellite (CGPS) observations of Rutford Ice Stream and Helheim Glacier indicate an appreciable phase shift between the ocean tides and the tidal perturbation in ice position (Gudmundsson, 2006; 2007; 2013; de Juan 2009; 2010a/b; and de Juan-Verger 2011). A zero degree phase shift corresponds to the case of the peak de-trended inland motion of the ice being synchronous with the high tide, with a positive phase lag indicating that the ground motion's peak response is delayed relative to the tidal peak. While our previous work suggests that the far-field observations of Rutford are probing a system other than the glacial rheology, the observations close to the grounding line of both Rutford Ice Stream and Helheim Glacier suggest that the phase lag is many tens of degrees. Equally important is that the phase delay may increase as a function of distance inland of the grounding line, suggesting that there is a calculable phase velocity to the propagation of the ice's response to the changing tides.

A phase lag to an oscillatory response is a classic characteristic of a viscoelastic material when the stress relaxation timescale is within several orders of magnitude of the forcing frequency (e.g., Findley et al., 1976). Given the forcing frequencies ranging from 12 hours to 14 days for the major tidal constituents, we expect that a material relaxation time between ~ 10^2 and ~ 10^8 seconds (~ 2 minutes to ~ 76 years) will result in a measurable phase shift, with the strongest phase response occurring when the relaxation time is approximately the same order of magnitude as the forcing frequency. This range matches the estimate of the linearized relaxation timescale for ice of approximately 10^2 to 10^4 seconds (~ 2 minutes to ~ 3 hours), based on the experimental work of Jellinek and Brill (1956) and the model fitting of Reeh et al. (2003).

We explore the feasibility and data quality necessary to provide constraints on the rheology based solely on the measured phase shift to a tidal forcing. This chapter starts with an analysis of the complex moduli of three canonical one-dimensional linear viscoelastic models in shear, focusing on the expected phase shifts as a function of the material parameters. We then investigate the phase response of nonlinear viscoelastic materials over a range of reasonable ice models for the nonlinear viscous deformation expected during steady-state tertiary creep. We then present results from two-dimensional finite element modeling exploring the spatial variability of a tidal phase shift and the role that model boundary conditions play in determining the spatial variation in any phase shift. We use these model results to provide a test case for determining the viscoelastic properties of ice using data from Helheim Glacier (i.e., from de Juan, 2009; 2010a/b; de Juan-Verger, 2011). We close this chapter with a discussion of the expected precision of the constraints on *in situ* viscoelastic parameters that tidal phase shift can provide and discuss factors necessary to select the ideal survey configuration and target.

4.2 Phase Shift in Analytic Models

Before exploring phase delay on a modeled outlet glacier, we first consider the behavior of three one-dimensional viscoelastic models—linear Maxwell, Kelvin, and Burgers—to an oscillatory forcing. These three models are shown schematically in the previous section (in figure 3.1). The Maxwell model is made up of a linear spring element and linear dashpot element in series, the Kelvin model is a linear spring and dashpot in parallel, and the Burgers model is a Maxwell element in series with a Kelvin element. The governing equations for these three models in shear are:

$$-\frac{\sigma}{\mu}+\frac{\dot{\sigma}}{\eta}=\dot{\varepsilon} \tag{4.1a}$$

$$\sigma=\mu\varepsilon+\eta\dot{\varepsilon} \tag{4.1b}$$

$$\sigma+\left(\frac{\eta_1}{\mu_1}+\frac{\eta_1}{\mu_2}+\frac{\eta_2}{\mu_2}\right)\dot{\sigma}+\frac{\eta_1\eta_2}{\mu_1\mu_2}\ddot{\sigma}=\eta_1\dot{\varepsilon}+\frac{\eta_1\eta_2}{\mu_2}\ddot{\varepsilon} \tag{4.1c}$$

where μ is the shear modulus, η is the viscosity, and, for the Burgers model, the subscripted 1 refers the Maxwell element and the subscripted 2 refers to the Kelvin element. We now apply an oscillatory shear load of frequency ω constant amplitude τ_0:

$$\sigma=\tau_0 e^{i\omega t} \tag{4.2}$$

We expect that the strain response will be oscillatory at the same frequency as the applied stress but shifted by a phase delay δ, such that:

$$\varepsilon=\varepsilon_0 e^{i(\omega t+\delta)}=\varepsilon^* e^{i\omega t} \tag{4.3}$$

Taking the ratio of strain to stress gives us the *complex creep modulus, J**:

$$J^* = \frac{\varepsilon}{\sigma} = \frac{\varepsilon^*}{\tau_0} = \frac{\varepsilon_0}{\tau_0} e^{i\delta} = J_1 + iJ_2 \tag{4.4}$$

Table 4.1 shows relevant values of J_1 and J_2, taken from Findley et al. (1976). We can also relate the phase shift to the components of J^* using:

$$\tan\delta = \frac{J_2}{J_1} \tag{4.5}$$

Lastly, we can define a natural timescale associated with each material model. For a Maxwell material, the stress due to a constant strain will decay exponentially with time, as controlled by the relaxation time T_{Max}. For a Kelvin material, a constant stress will induce a creep strain that exponentially approaches the equivalent elastic strain. The timescale of this creep is controlled by the retardation time, T_{Kelv}. In the Burgers model, there is both a relaxation time T_{Burg1} and a retardation time T_{Burg2}. The values of these natural timescales are shown for each model in table 4.1.

4.2.1 One-Dimensional Phase Shift

We are now equipped to determine the expected phase shift for a given material model of ice for a forcing function of known frequency. However, as there are two separate free parameters (the appropriate relaxation/retardation timescale and the forcing frequency), we again introduce the Deborah number, *De*:

$$De = \frac{T_R}{T_F} \tag{4.5}$$

where the Deborah number is the ratio of a material's relaxation time to the period of an applied forcing. When *De* is large, the material behaves elastically, when *De* is small, the material behaves viscously, and when *De* is around one, the material behaves viscoelastically. The Deborah number encapsulates the choice of the material parameters (shear modulus and viscosity) and the forcing frequency, allowing us to calculate the phase shift with respect to a single nondimensional quantity.

Figure 4.1 shows the phase shift in the strain response to an oscillatory stress for the linear Maxwell, Kelvin, and Burgers models (assuming $\eta_1 = \eta_2 = \eta$ and $\mu_1 = \mu_2 = \mu$). From this figure, we see that all the linear models predict a phase shift between 0 and 90 degrees, with the Maxwell and Burgers models predicting the phase shift to increase at small *De* while the Kelvin model demonstrating a larger phase shift at large *De*. All three models meet at a phase shift of 45 degrees, when $De \approx 10^{-0.8} = 0.158$.

As seen in the linear phase curves, the Maxwell and Burgers models act most similarly to the expected phase response, where a material that behaves more viscously than elastically will have a stronger out-of-phase displacement response than a comparatively more elastic model. Thus, the Kelvin model, a representation of a solid material, is a poor model choice for phase shift in ice and will not be considered further. Second, while the trend in phase is distinct between the Maxwell and Burgers models, a large number of high quality data would be necessary to adequately distinguish between these two models. As the constraining data in $\delta - De$ space should only vary with tidal frequency, any rheological fitting would be based on, at best, a handful of observations with different *De*. Thus, given the relative sparsity of our expected data and the fewer numbers of parameters, we choose to continue our investigation of ice rheology by assuming a Maxwell material for the ice response to a tidal load.

4.2.1Phase Shift for a Nonlinear Maxwell Material

The nonlinear viscosity of ice complicates the understanding of the phase shift in the oscillatory response of a one-dimensional nonlinear material model. We explore the phase shift in a nonlinear Maxwell model with the nonlinearity limited to the viscous component of deformation, such that the constitutive law is given by:

$$A\sigma^n + \frac{\dot{\sigma}}{\mu} = \dot{\varepsilon} \tag{4.6}$$

where n is the power law exponent and A is the nonlinear viscosity coefficient. Note that for these simple models, the temperature dependence of A is neglected. The approach used in the previous section to calculate the phase shift δ becomes untenable for an oscillatory nonlinear model as the effective linear viscosity would necessarily oscillate with the forcing function amplitude, resulting in a time-dependence on the phase shift. Instead, we adopt a different method to finding the one-dimensional phase shift for our nonlinear Maxwell model.

First, we choose the periodicity of the stress forcing function to match that of the three major tidal constituents, rounded to the nearest integer hour: 12 hours for the semidiurnal tide, 24 hours for the diurnal tide, and 14 days for the fortnightly tide. We then solve for the strain rate of each of these tides, as well as the linear combination of the three tides (a “combined tide” forcing), using equation 4.6. The values of A and n used in this analysis match the values from the Glen and Goldsby rheological models for ice at 0°C in tertiary creep (Glen, 1955; 1958; Goldsby and Kohlstedt, 1997; 2001), and μ from the canonical values of E and ν (Petrenko and Whitford, 2002). As we are forcing our tides at a known period and the longer tides are integer multiples of the shorter tides, we can use a Fourier analysis to find the exact phase for the applied forcing functions. Lastly, shifting the phase of the strain rate by 90° gives us the phase delay in the modeled strain as the strain rate is the time derivative of strain.

The phase shift values for the semidiurnal, diurnal, fortnightly, and combined tides are shown in figure 4.2 as functions of *De* and for a linear, Glen, and the two Goldsby rheologies. For all the models, the expected phase shift trends are fairly similar, and the value of δ ranges from 0° to 90°. At a given tidal frequency, the predicted phase shifts are independent of the material parameters. A single forcing frequency will not perturb the amplitude of the forcing function, and thus will not change the effective viscosity of the material. However, as highlighted in table 4.2, the combined tide does show a nonlinear effect on the phase of any given tidal constituent, such that some of the phase shifts are slightly elevated or depressed for a given *De* compared to the value for the individual tidal frequency. The value of *De* for a given phase shift can vary by as much as a factor of two for the rheologies considered here. With the stress-dependent rheology, the discrepancy between the phase shift when the model is forced with the individual tides compared to the combined tides is more severe the higher the power law exponent is.

4.3 Two-Dimensional Finite Element Models

Having established some intuition for the phase shift from our one-dimensional models, we now present results from a range of two-dimensional, nonlinear Maxwell finite element models exploring the phase shift of a higher dimension viscoelastic body to an oscillatory force. First the variation in observable surface phase shift is categorized as a function of the modeled ice streams' boundary conditions, the choice of rheology, and the spatial variability of the phase shift across the model's profile. Then, this model approach is validated using data from Helheim Glacier to estimate viscoelastic parameters for ice. Such parameters are found to be within a range compatible with laboratory values for ice viscoelasticity.

4.3.1 Methodology

As with our earlier models, we use the *PyLith* software package (as described in section 1.4) for our finite element modeling. The model geometry is a simplified version of the lower portion of Helheim Glacier (750 meters thick and six kilometers wide). We explore two different model boundary conditions in our analysis, as are shown in figure 4.3. First is the case of an outlet glacier that is stuck to its bed, such that the controlling dimension is the ice thickness. This model is equivalent to the “frozen bed” model from chapter 2. Second is a two-dimensional outlet glacier that is stuck to its lateral margins. For each of models, we apply the tide as an oscillatory traction boundary condition along one edge of the model domain. As discussed above, we choose to model a single tidal frequency at a time, rather than combining tides of multiple frequencies.

4.3.2 Numerical Results

Figures 4.4 and 4.5 show the behavior of the phase for our basal and side-wall models, respectively, as a function of *De*. In figure 4.3, our models show the phase at the grounding line and at locations one, two, and three kilometers inland, while figure 4.5 includes the grounding line and locations five, ten, fifteen, and twenty kilometers inland. The difference in length-scale is needed because the side-wall models have a larger decay length-scale, L_{tr}, than the basal models. In each figure, we include model results for a linear viscoelastic model (shown in blue) and nonlinear viscoelastic models (other colors) forced at multiple tidal frequencies. For the basal model, the only nonlinear model considered has a power law exponent of $n=3$, while for the side-wall models, we also consider *n=1.8* and *n=4*. These three power laws correspond to the rheologies associated with a Glen flow law (Glen, 1955; 1958), superplastic flow (Goldsby and Kohlstedt, 1997; 2001), and climb-limited dislocation creep (Goldsby and Kohlstedt, 1997; 2001). Due to the exceedingly small stable timestep in the low-viscosity nonlinear models, the range of *De* explored is more limited than for the linear case.

For both model boundary conditions, the linear models demonstrate the arctangent form of the phase-Deborah number relationship produced analytically for a one-dimensional Maxwell material, with the phase ranging from zero degrees (elastic behavior) to ninety degrees (viscous behavior). The change in the material behavior occurs over a range of about two and a half orders of magnitude—such that $10^{-2.5} < De < 10^{0}$. However, unlike the one-dimensional case, in the region where the phase is neither zero nor ninety, the phase shows a dependence on distance from the grounding line, as demonstrated by the spread in phase values over the locations shown in figure 4.4 and 4.5.

To better demonstrate this distance dependence, figures 4.6 and 4.7 show the phase shift of the centerline ice as a function of inland distance (note that the horizontal length-scale varies due to the difference in L_{tr} between the two models). These two figures are remarkably similar, suggesting that the expected phase shift trend with inland distance, at least in a two-dimensional model, is not dependent on the absolute distance away from the grounding line but rather on the relative strength of the tidal signal. Appendix 4A shows the phase shift seen across the model domain for the side-wall models.

For each model, the nonlinear solutions are shifted to the left (i.e., towards lower *De*) compared to the corresponding linear viscoelastic model. This behavior matches that of the one-dimensional solution. As seen in both figures 4.3 and 4.4, the solutions for a given rheology at different tidal frequencies agree fairly well, confirming that the Deborah number is a controlling parameter of the phase shift. Another implication of the dependence on *De* is that phase data collected for multiple tidal frequencies will provide multiple data points along the same curve, rather than each tidal frequency belonging to unique functions.

Unfortunately, the models presented here are insufficient to provide a well-constrained fit to the arctangent form of the phase response of each model to the applied oscillatory loads. In the case of the linear model, such a deficiency could be addressed through filling out the model space through additional modeling. For the nonlinear scenarios, the finite element models for the lowest values of *De* are already on the verge of taking too long to run to be computationally viable. These models currently take about one week per model, and are not easily parallelizable due to the sequential nature of timestepping. Thus, every order of magnitude decrease in *De* would increase the run time by approximately an order of magnitude, as the stable timestep of the Maxwell rheology is small enough (compared to the forcing function) to require extensive calculations for even a single tidal cycle. Thus, we suggest that extrapolating the linear trend onto the nonlinear data would provide an estimate for the nonlinear viscoelastic response at these lower values of *De*. For the purposes of demonstration here, we assume that the phase varies linearly between the data points. This approach is clearly inadequate, but as we lack the model results necessary for an accurate functional fit to the phase points, such an approach is a practical alternative to a poorly constrained arctangent function.

4.3.3 Application to Helheim Glacier Data

We now present a simple test example of using ice stream phase data to provide constraints on the viscoelastic properties of ice. For our purposes, we use calculated phase delays from Helheim Glacier (de Juan, 2009; 2010a/b; de Juan-Verger, 2011) as our dataset, even though the errors for the phases can quite substantial. For each of the three surveys from de Juan-Verger, the data point closest to the grounding line is used to approximate the phase response at the grounding line, so that the distance dependence of the phase response can be negated. While de Juan-Verger (2011) presents linear extrapolations of the phase measurements to the calving front of Helheim Glacier, we choose to use the closest data point rather than the extrapolated value due to the large data uncertainties influencing the linear fit. For the three surveys, the phase differences are $27° \pm 3°$, $53° \pm 15°$, and $55° \pm 15°$.

Figure 4.8 shows the location of these phases on the basal model (panel A) and the side-wall model (panel B), with the values of the fitted effected viscosities listed in table 4.3. The fits are relative to the linear model (blue) and the extrapolated nonlinear model for $n=3$ (red). The extrapolated line is found by shifting the linear model by a constant offset until the new line matches the finite element values for the nonlinear phase shift. The differences between the predicted values of the effective viscosities are minimal between the two models. In all cases, T_{Max} is on the order of 10^2 to 10^3 seconds (~2 to ~20 minutes), though the variation between the lowest and highest estimates differs by a factor of about 60. Assuming a Young's modulus of 9.33 GPa (Petrenko and

Whitford, 2002), the estimates of the ice viscosity from these Helheim Glacier phases data fall between $1.01e12\ \mathrm{Pa \cdot s}$ and $5.83e13\ \mathrm{Pa \cdot s}$. Considering the uncertainty in our model trend and the wide range in errors of the Helheim phase data, these values are remarkably close to the estimated linear viscosity value for ice of Jellinek and Brill (1956) of $1e12\ \mathrm{Pa \cdot s}$ to $1e14\ \mathrm{Pa \cdot s}$ for similar stresses.

In this brief demonstration, the distance dependence of the solution is not considered, as the phase data from Helheim Glacier is not constrained enough to adequately show a convincing distance dependence. However, as our work demonstrates, the distance dependence of the phase is diagnostic of the ice's material properties, such that if the phase data is accurate, the variation in phase with distance inland of the grounding line could potentially differentiate between rheologies (i.e., n could be fit, rather than assumed).

4.4 Discussion

While our model for constraining the viscoelasticity of *in situ* ice is fairly rudimentary, our ability to get close to the expected value of effective viscosity using a few, somewhat unconstrained data points and a suboptimal suite of models is encouraging. In this section, we first focus on the expected accuracy of the material parameter estimates found by the approach outlined here. We then provide a blueprint for an ideal survey to collect data necessary to constrain rheological parameters of ice streams, including a discussion of the characteristic of an outlet glacier that would make that glacier a prime survey target.

4.4.1 Data Constraints and Accuracy

As only two data sets exist in the published literature quantifying the observed tidal phase shift from ice streams, quantifying the relative error within the current dataset is relatively straightforward. Gudmundsson (2006; 2007; 2011) used the MATLAB script *T_TIDE* (Pawlowicz et al., 2002) to solve for the phase delays in the Rutford Ice Stream GPS records over a range of tidal frequencies to an accuracy of about +/- 8°. Gudmundsson's GPS survey lasted for seven-weeks, providing several fortnightly periods and many dozens of diurnal and semidiurnal tidal periods. De Juan-Verger (2011) estimated the phase delay in the Helheim Glacier GPS network for the semidiurnal tide. The accuracy of the phase delay in those data ranged from +/- 3° to as much as +/- 90°. The survey near the grounding line for Helheim Glacier only lasted for between 2 and 5 days, depending on the site location.

The error in the estimated ice Maxwell time is directly related to the error in the phase estimate. Due to the arctangent form of the phase as function of Deborah number, when the phase is close to either zero or ninety degrees, even a small error in the phase can result in several orders of magnitude in uncertainty in the estimated value of *De*. Conversely, when the measured phase is around 45°, the range in *De* for a given error in phase is small. For example, there is less than one order of magnitude change in *De* for phase shifts ranging from 15° to 75°.

Recall that our two-dimensional models all have a phase shift bounded between 0° and 90° relative to the forcing function. In both the observations of Rutford Ice Stream (Gudmundsson, 2006; 2007; 2011) and the viscoelastic three-dimensional models presented earlier in chapter 3, the phase of ice response was greater than 90°. Phases greater than 90° cannot result from the two-dimensional models in this chapter but are seen in the three-dimensional viscoelastic models shown earlier in chapter 3. Thus, our two-dimensional models are necessarily over-simplifications to the phase behavior of ice streams. However, for a rough estimate of the viscoelastic properties, these two-dimensional models provide a general constraint on the rheology. A more accurate estimate of the viscoelastic material parameters would require the use of a three-dimensional viscoelastic model specific to the target glacier.

4.4.2 Survey Requirements

As the number of studies demonstrating a tidal phase delay is limited to only a handful, the collection of more data would aid in the understanding of *in situ* ice rheology. As such a study necessarily would focus on the surface response of a tidally-forced ice stream, the survey would be geodetic in nature. From our modeling, the most important phase constraint is the phase delay near the grounding line, where the stresses (and thus displacements) caused by the tides are at a maximum. In the case of an ice stream primarily constrained by its lateral margins, our work in chapters 2 and 3 suggests that a geodetic survey should remain within three ice stream widths of the grounding line. Farther inland, the tidal forcing is expected to be at least two orders of magnitude smaller than at the grounding line, which is likely too small to be detectable above the background ice velocity. Our modeling also suggests some lateral variation in the observable phase shift (see appendix 4A), especially for a nonlinear viscoelastic rheology. Therefore, we suggest that a grid pattern of geodetic stations would be an ideal deployment, as both the lateral and inland variations in phase shift would be recorded.

As the fitting of the tidal amplitudes and phases has been shown to be fairly rough (at best within a few degrees), the positional accuracy of the GPS survey is not expected to be an important concern relative to the error in fitting the tidal phase. Due to the rugged nature of the lowest reaches of many ice streams, deploying relatively inexpensive (perhaps even expendable) GPS stations is preferred as there is a nontrivial chance that any given station would be lost due to iceberg calving, crevassing, or some other potentially destructive ice process. Due to the inherent instability of the ice, using geodetic satellite observations would seem like a good alternative to on-ice geodetic stations. However, the repeat time between satellite orbits is probably too long to sufficiently resolve semidiurnal and, perhaps, the diurnal tides.

Another consideration would be the duration of the survey. Ideally, the survey would be as long as possible, as the longer the survey duration, the better the estimates of the periodicity and phase delay of the ice response would be. While the difference in the size of the errors between Gudmundsson (2006; 2007; 2011) and de Juan-Verger (2011) is not due to the difference in survey duration alone, the shorter survey of de Juan-Verger certainly does not help estimate the phase. Independent of the estimation errors, longer surveys provide the opportunity to use the longer period ocean tides as additional data points for fitting the phase in $\delta - De$ space. We recommend that a survey long enough to capture two full fortnightly periods would be a minimum survey duration for a rheologically motivated study.

Given the high rate of ice motion in ice streams and outlet glaciers, a one-month timeframe puts a limit on how close stations could be placed to the grounding line without the ice carrying the station past the grounding during the course of the observation period. Assuming a maximum ice velocity of 11 km/yr (for Helheim Glacier, Thomas et al., 2000; Howat et al., 2005), the nearest to the calving front that a recording station for a month-long survey could safely be placed is about 850 meters inland. For ice streams with an attached ice shelf, while the GPS station would not be lost if carried past the grounding line, the nature of the station's phase response would necessarily change if the ice beneath it begins to float. Such a dramatic change in ice behavior could greatly increase the difficulty in interpreting the ice properties from the phase data.

Lastly, the methodology for determining viscoelastic properties discussed here only provides information about the relaxation time of the glacier, rather than an intrinsic value of either the effective viscosity or the Young's modulus. Recall that the viscosity for our test problem in section 4.3.3 could only be found by assuming the Young's modulus matched the laboratory value (from Petrenko and Whitford, 2002). However, as the density of ice is a well-constrained material property (e.g. Cuffey and Paterson, 2011), the acoustic wave speed within an ice stream can provide a constraint on the value of Young's modulus for ice independent of the phase delay. Glacial seismicity happens regularly enough to be used as a reliable source of acoustic waves in outlet glaciers. As a range of possible glacial earthquake sources have been suggested (e.g., Neave and Savage, 1970; VanWormer and Berg, 1973; Weaver and Malone, 1979; Wolf and Davis, 1986; Qamar, 1988, Anandakrishnan and Bentley, 1993; Anandakrishnan and Alley, 1997; Deichmann et al., 2000; Ekström et al., 2003; Stuart et al., 2005; Smith, 2006; O'Neel et al., 2007; Tsai and Ekström, 2007; Tsai et al., 2008), the best approach would be to have an array of seismic monitoring stations that could measure the relative arrival time between stations of a wave, and thus estimate the wave speed independent of the source location. From the wave speed, the average ice density could then be used to determine the ice's elastic moduli. Such a seismic array would not need to be placed close to the grounding line, and a wide coverage might even be ideal due to the increased travel times of various waves increasing the accuracy of estimating ice's elastic parameters.

4.4.3 Ideal Survey Targets

Equally important as the survey configuration is the choice of glacier to target for a rheologically-motivated tidal phase study. From our analysis of simple models, as well as the results presented earlier in chapters 2 and 3, we propose a series of criterion for selecting a glacier most likely to provide data of a high enough quality to constrain *in situ* viscoelastic parameters. Such criteria include the type of glacier to study, the nature of the ocean-ice interaction, the geometric complexity of the target glacier, and the thermal characteristics of the glacier. Each of these selection characteristics will be discussed separately.

4.4.3.1 Glacier Type

Glaciers exhibit a wide range of geometries, sliding velocities, boundary conditions, and ice properties. Ice streams make a natural target for a tidal phase survey as these glacier have the benefits of being fast moving, of having large ice fluxes, and of all having continuous contact with the ocean. The rapid ice velocity makes distinguishing between the secular flow rate and a tidally-perturbed signal more straightforward than for an equivalent slow moving glacier. In cases where the rapid ice motion is due to low resistive stresses, we expect a larger region where the tidal perturbation is measurable than for slower moving glaciers. The large ice flux also ensures that the glacier is always in contact with the ocean, such that the tidal interaction does not "turn off" as a function of time. Lastly, and perhaps most importantly, the surveys of Rutford Ice Stream and Helheim Glacier demonstrate that a phase lag on ice streams is measurable. Such may not be the case for other types of tidewater glaciers, where the existence of a tidal perturbation to ice motion, let alone the existence of a phase lag in that perturbation is not yet established.

4.4.3.2 Ocean-Ice Interaction

From the observations summarized in the introduction of chapter 2, glaciers can be grouped into three categories based on the glacier's response to a tidal perturbation: little to no tidal response, measurable perturbation in the ice stream's displacement, and stick-slip response to ocean tidal loading. Clearly, given the need for a signal and the desire to avoid unnecessary complications, the ideal target glacier would, the ideal target glacier resides in the second category. Such glaciers are expected to show a perturbation in surface displacement that varies smoothly in response to a change in tidal amplitude.

Additionally, the presence of an ice shelf is a key consideration in determining the interaction between an ice stream and the ocean tide. For a tidewater (i.e. shelf-free) glacier, the change in ocean tide acts only as a change in the water pressure acting on the glacier's ocean-ward cliff. For a glacier with an attached shelf or tongue, the rise and fall of the ice shelf introductions flexural stresses on the glacier in the first five to ten kilometers (i.e., ice thicknesses) of the grounding line (as demonstrated in chapter 2, appendix 2A and observations in table 2.1). While our determination of the stress transmission length-scale of ice streams shows that the tidal stress can influence ice stream motion farther inland than ice flexure will for a wide enough glacier, the added flexural stresses of an ice shelf will influence the value of the stress-dependent effective viscosity, complicating the determination of the ice viscosity. The 2007-2008 data from de Juan-Verger's (2011) study of Helheim Glacier demonstrates that an ice shelf is not a critical factor in determining the phase shift between an ice stream and the ocean tide, we suggest that a target glacier should not have an ice shelf.

4.4.3.3 Geometric Complexity

Glaciers span a wide range of morphologies, from being a single linear feature to being a meandering convergence zone of multiple glacial streams. A prime target glacier would be nearly linear and sourced from a single region of ice. From a geometric perspective, a complex flow field is expected to differ from our simple, linear models due to the geometry alone. Additionally, if a glacier is made up of multiple ice sources coalescing into a single flow near to the grounding line, the possibility of rheological variations across its profile becomes greater. Such lateral variations could influence the phase shift seen on the ice stream, such that the estimated viscoelastic parameters are representative of neither ice constituent but rather some bulk average. While such a result is not wrong *per se*, the apparent viscoelastic parameters would be useful only to that one system and could not be used as a general measurement of *in situ* glacial ice rheology.

Glaciers also can be underlain by deformable till (soft bedded) or by undeformable rock (hard bedded). The two-dimensional models in this chapter and the three-dimensional models in chapter 3 demonstrate that the choice of boundary condition acting on the glacier is important to determining the precise phase-shift due to the rheology. While both soft and hard bedded glaciers are likely to have boundary-specific modifications to the phase shift that need to be distinguished from rheological effects, the added material of the subglacial till in soft bedded glaciers presents an additional constitutive law necessary to understand any observed phase shift. Thus, soft bedded glaciers are more complex than their hard bedded counter parts, leading us to suggest that an ideal test glacier would be hard bedded.

4.4.3.4 Thermal Complexity

Glaciers fall into two categories based on the nature of the temperature of the ice: isothermal warm glaciers and polythermal cold glaciers. As discussed in chapter 3, the ice streams of Antarctica (and Greenland) are definitively polythermal, with basal temperatures as much as twenty degrees warmer than the surface temperatures. Most other glaciers on Earth, by their nature of being much smaller, are isothermal, with the ice at the melting temperature throughout the glacier. As ice viscosity is strongly temperature dependent (e.g., Nye, 1953; Jezek et al., 1985; Budd and Jacka, 1989; MacAyeal et al., 1996; 1998) and ice elasticity weakly temperature dependent (Jellinek and Brill, 1956), an ideal target glacier would be isothermal, where the confounding effects of temperature could be avoided.

4.4.3.5 Ideal Target Selection

Using the above criteria, we compile a list of ice streams in table 4.4 that would be potential targets for a rheologically-motivated GPS survey. This table focuses on major ice streams and outlet glaciers in a range of environments, including: Bindschadler Ice Stream, Ekstrom Ice Shelf, Kamb Ice Stream, Pine Island Glacier, Thwaites Glacier, Whillans Ice Plain (Antarctica); Helheim, Kangerdlussuaq, Jakobshavn Isbrae glaciers (Greenland); Columbia and LeConte glaciers (Alaska). Among these major ice streams, there is not a single “perfect” target glacier. The best targets are Columbia Glacier, Alaska and Helheim Glacier, Greenland due to confirmed tidal interactions, rapid ice motions, a lack of an ice shelf, and the confining nature of these fjord-bounded glaciers.

Of special importance is that these ice streams have no ice shelves, as shelf-less glaciers have a much simpler tidal forcing configuration and thus a less involved calculation of the tidal phase. An ice shelf adds the complications of ice flexure and grounding line migration to the tidal perturbation of ice velocities. Detailed modeling work of the interplay between the grounding line and ice shelves demonstrates that the stress and deformations of glaciers near the grounding line are inexorably tied to these shelf behaviors (e.g., Schoof, 2007a/b; Goldberg et al., 2009; chapter 2 of this thesis). Ultimately, we suggest that the single strongest selection criterion should be the presence (or lack) of an ice shelf.

4.5 Summary and Conclusions

In this chapter, we outlined a methodology for inferring the viscoelastic properties of an ice stream from the phase shift in the ice stream’s response to the forcing of the ocean tides. From our modeling, a phase delay is expected when the value of *De* falls between 10^{-3} and 10^{1}. While the models used here to calibrate the relationship between phase and rheology are simple two-dimensional models, our ability to use these models in conjunction with observations from Helheim Glacier to estimate a reasonable value of viscosity suggests that using the phase lag to invert for the *in situ* material properties of ice could produce meaningful results. While more detailed analysis is beyond the scope of this work, we outline a potential observational campaign to constrain ice rheology. Lastly, while the previous two chapters discussed ways in which the tidal loading of ice have been modeled inappropriately, this chapter highlights the potential use of the short-timescale geodetic observation of ice stream’s response to ocean tides to constrain the viscoelastic properties of natural glacial ice.

	Variable Names	Units
A	Viscoelasticity coefficient	Pa^{-n} s^{-1}
De	Deborah number	--
$J*$	Complex creep modulus	Pa^{-1}
J_1	Real part of $J*$	Pa^{-1}
J_2	Imaginary part of $J*$	Pa^{-1}
L_{tr}	Transmission length-scale	km
n	Power law exponent	--
T_F	Forcing function period	s
T_{Burg1}	Burgers relaxation time (Maxwell element)	s
T_{Burg2}	Burgers retardation time (Kelvin element)	s
T_{Kelv}	Kelvin retardation time	s
T_{Max}	Maxwell relaxation time	s
T_R	Relaxation time (general)	s
t	Time	s
δ	Phase delay	°
ε	Strain	--
$\varepsilon*$	Complex Strain	--
ε_0	Strain amplitude	--
η	Linear viscosity	Pa s
η_1	Maxwell element viscosity (Burgers body)	Pa s
η_2	Kelvin element viscosity (Burgers body)	Pa s
μ	Shear modulus	Pa
μ_1	Maxwell element shear modulus (Burgers body)	Pa
μ_2	Kelvin element shear modulus (Burgers body)	Pa
ν	Poisson's ratio	--
σ	Stress	Pa
τ_0	Stress amplitude	Pa
ω	Frequency	s^{-1}
" $\dot{}$ "	Indicates time derivate	

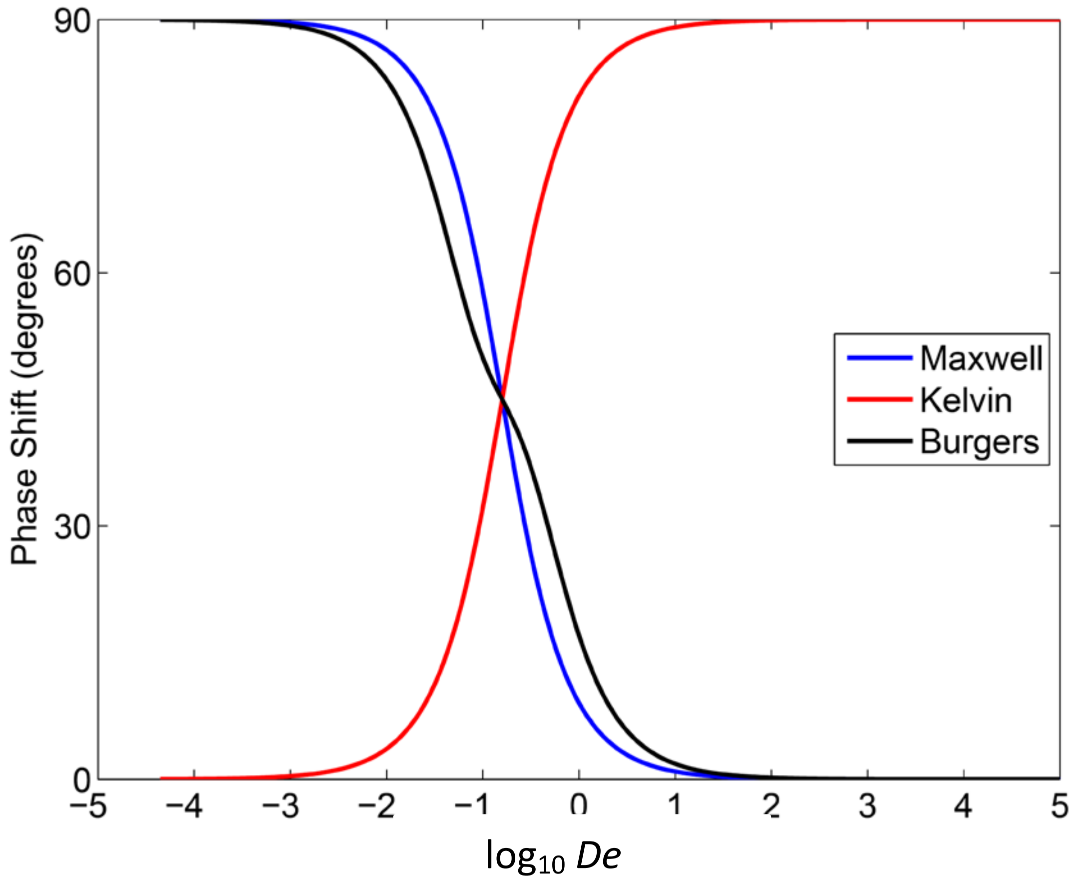

Figure 4.1: Diagram showing the phase delay in the response of a one dimensional Maxwell (blue), Kelvin (red), and Burgers (black) viscoelastic element, as a function of the Deborah time of that model.

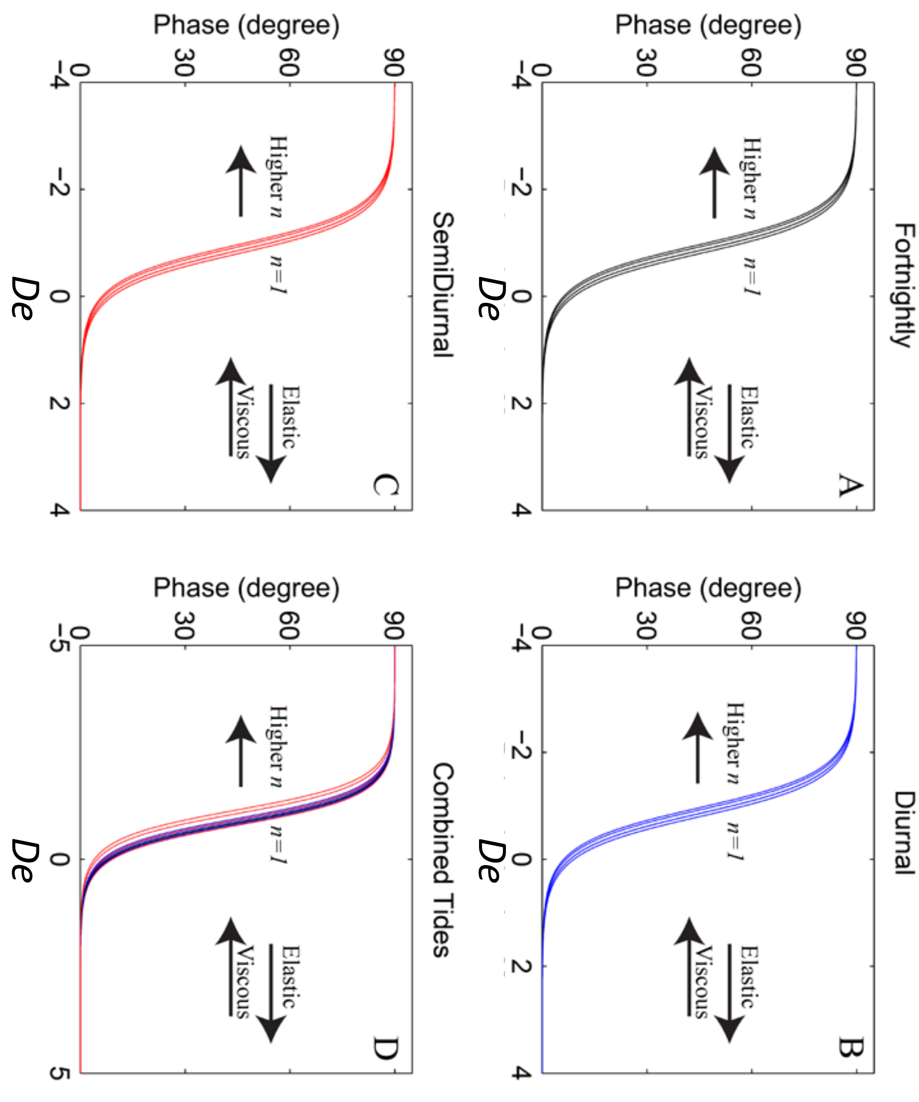

Figure 4.2: Phase shift for linear and nonlinear Maxwell models over a range of forcing frequencies and rheologies. Panel A shows results for the fortnightly tide (black), panel B the diurnal tide (blue), panel C (red), and panel D the combined tide (all three colors). In all cases, the lines represent increasing values of *n* from right to left. Values in table 4.2 are collected from figure 4.2D, and will aid in distinguishing the different behaviors of each tidal signal as part of the combined tide.

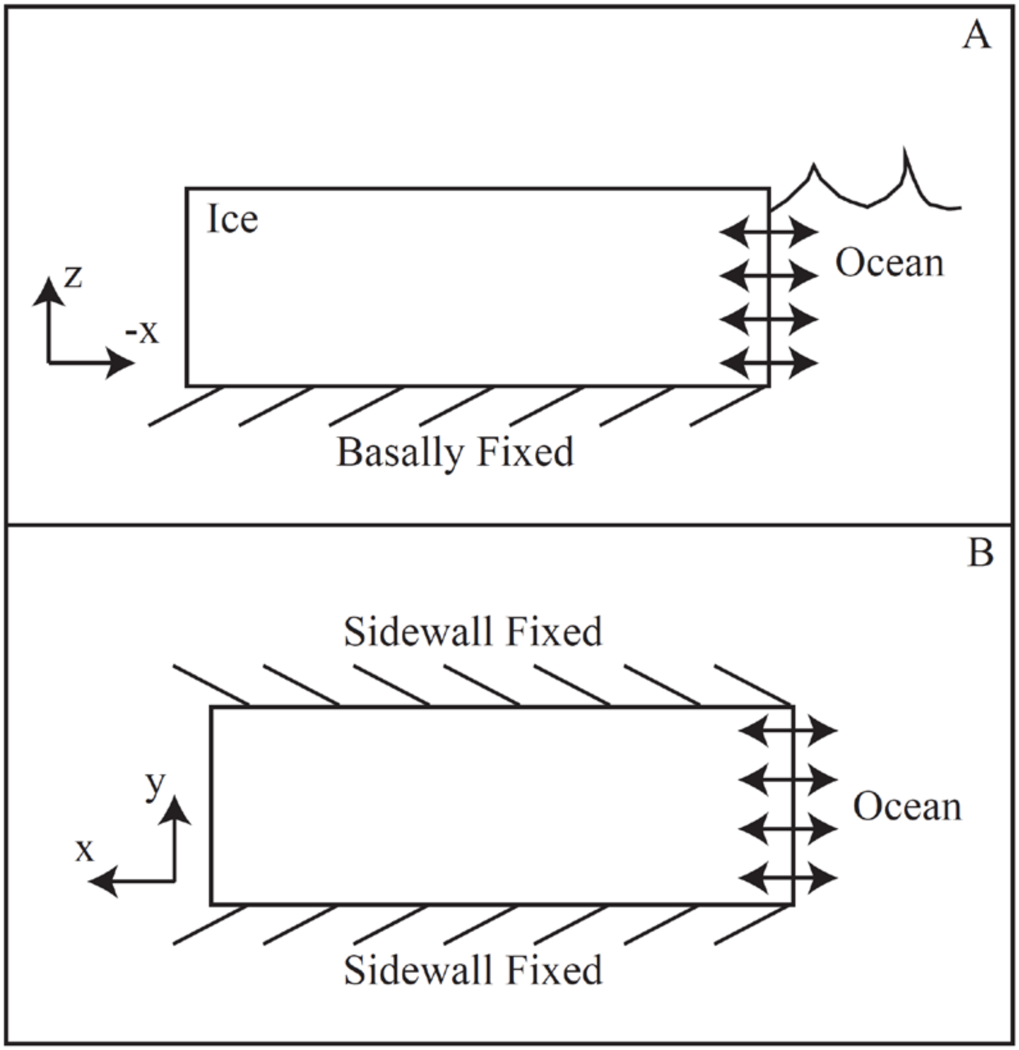

Figure 4.3: Schematic diagrams of the two model configurations for our finite element models. Panel A shows a vertical cross-sectional view of a model ice stream that is fixed at its bed. Panel B shows a map view of an ice stream that is fixed on each lateral margin. The arrows show the location of the applied tidal forcing function.

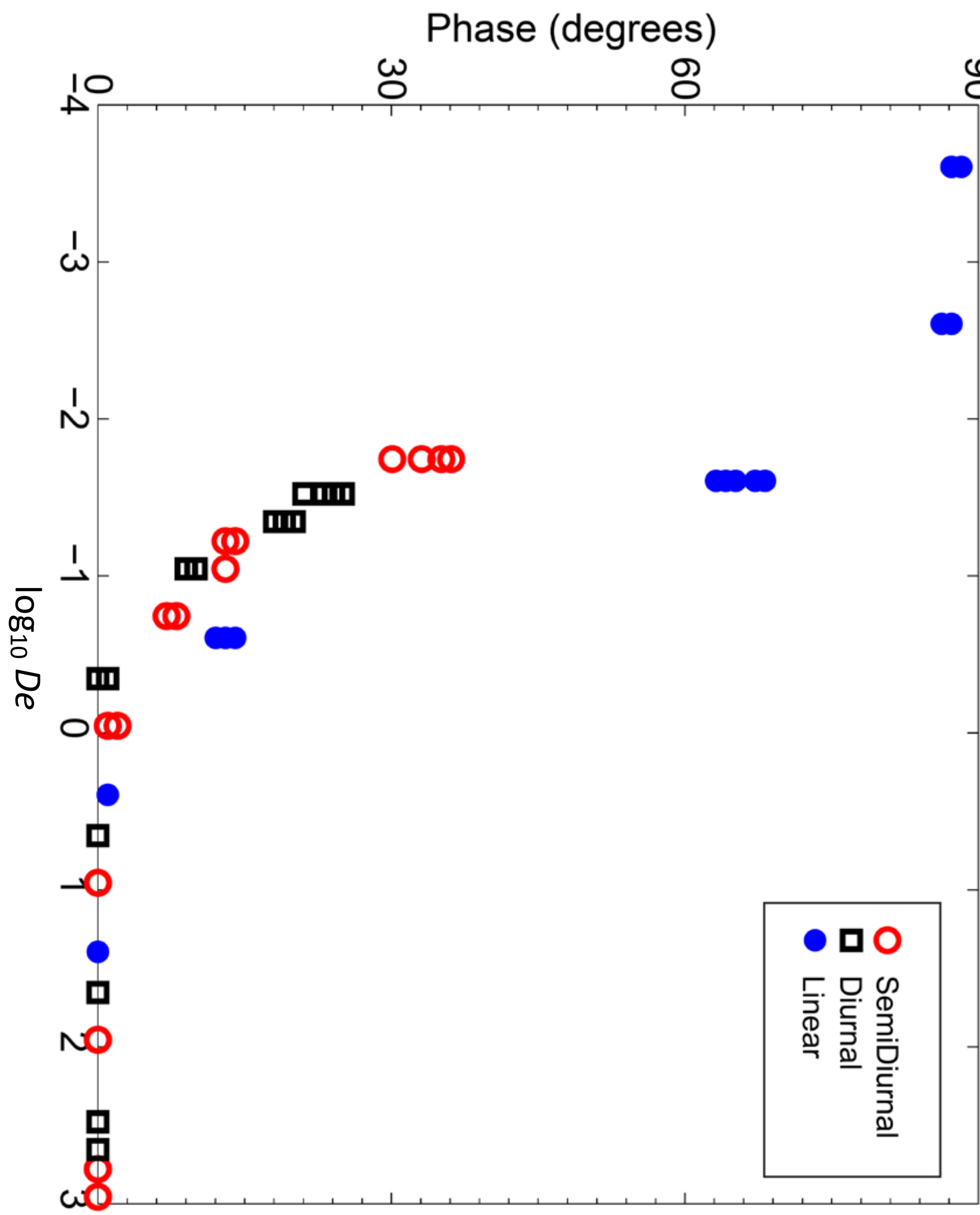

Figure 4.4: Modeled phase shift results for our models fixed at the bed (see figure 4.3A). The filled blue circles show the results for a linear Maxwell model, while the red circles and black squares show results for a nonlinear Maxwell model with *n=3* forced by a semidiurnal and diurnal tide, respectively.

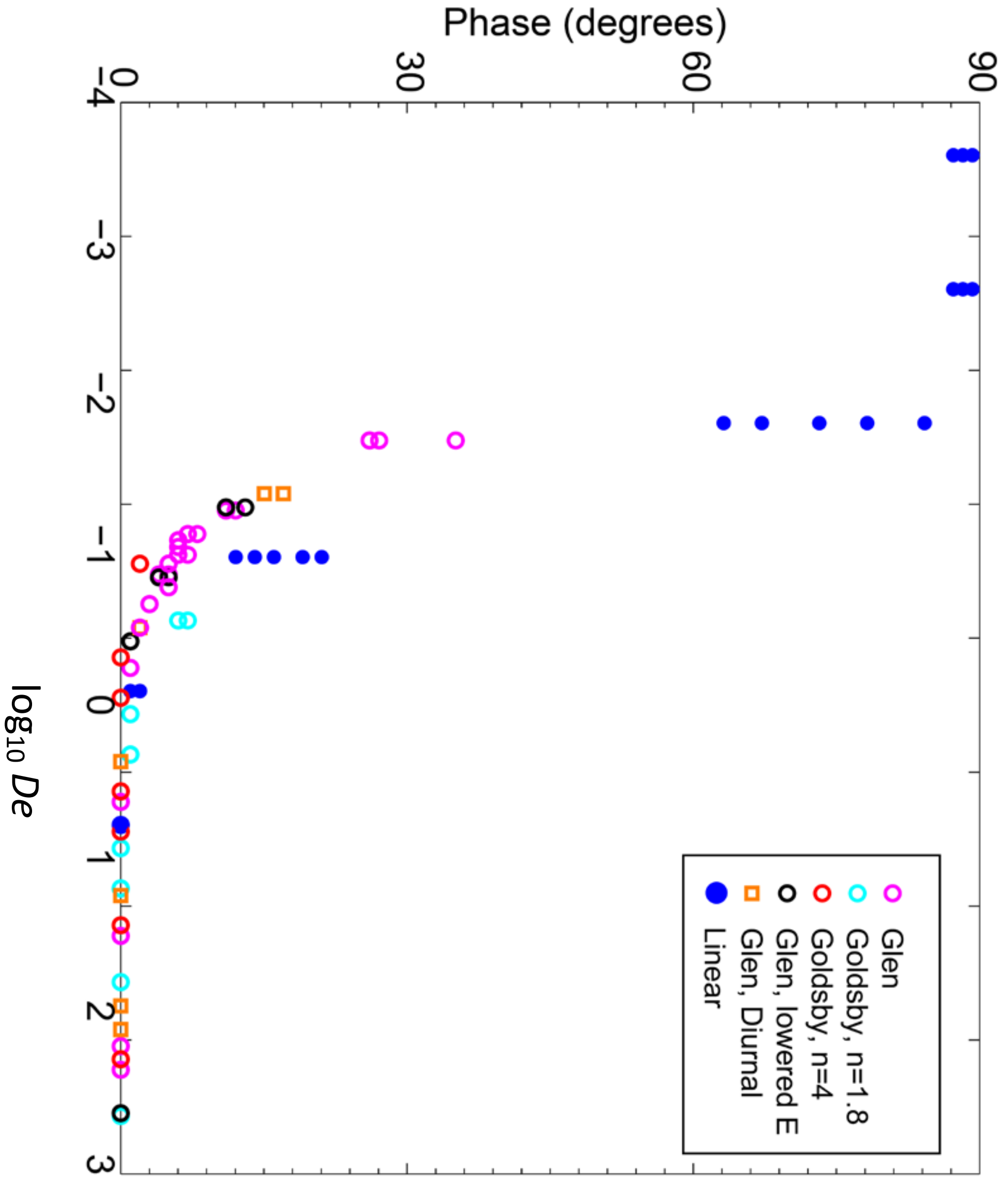

Figure 4.5: Modeled phase shift results for our models fixed on the side walls (see figure 4.3B). The filled blue circles show the results for a linear Maxwell model, while all the open circles represent nonlinear models forced with a semidiurnal tide and all squares represent nonlinear models forced with a diurnal tide. The colors correspond to a Glen rheology (pink, black, and orange), a Goldsby rheology with *n=1.8* (light blue), and a Goldsby rheology with *n=4* (red).

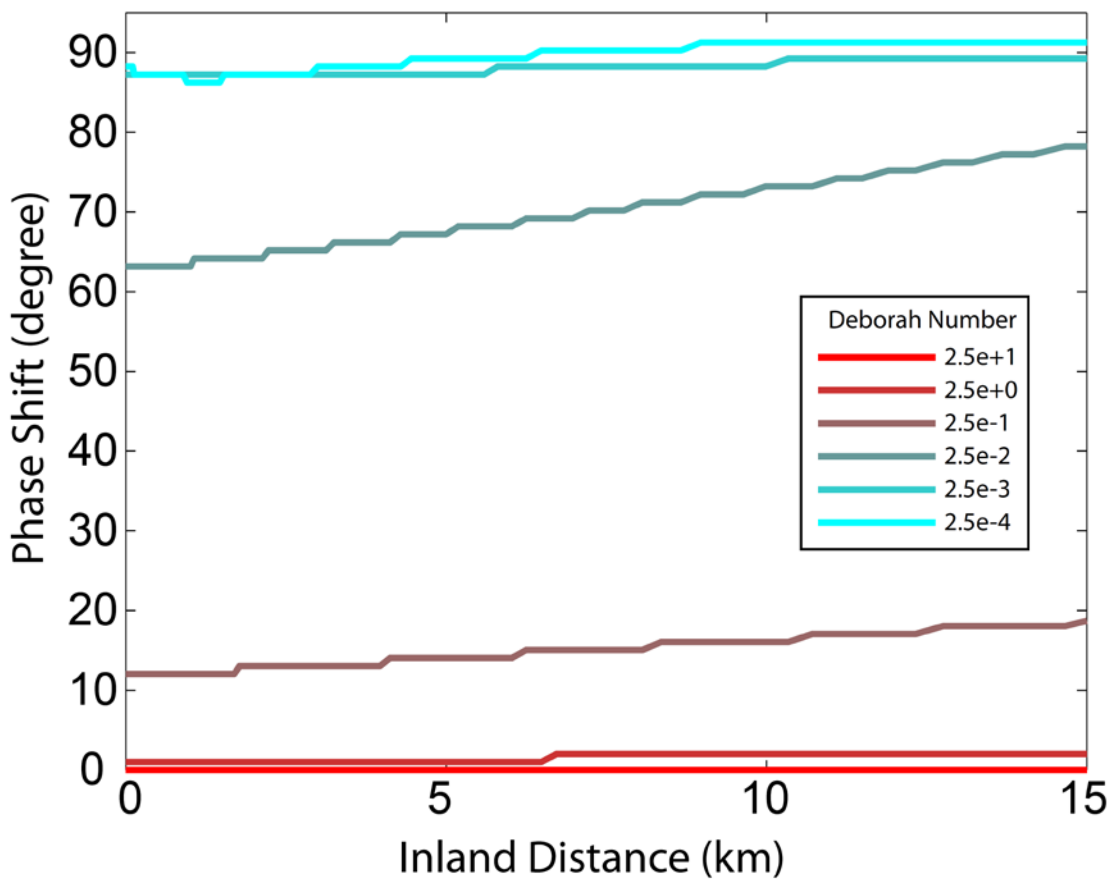

Figure 4.6: Distance dependence of the phase shift for basally-locked models at a range of Deborah numbers. The redder colors represent more elastic models (higher *De*) while the bluer colors represent more viscous models (lower *De*).

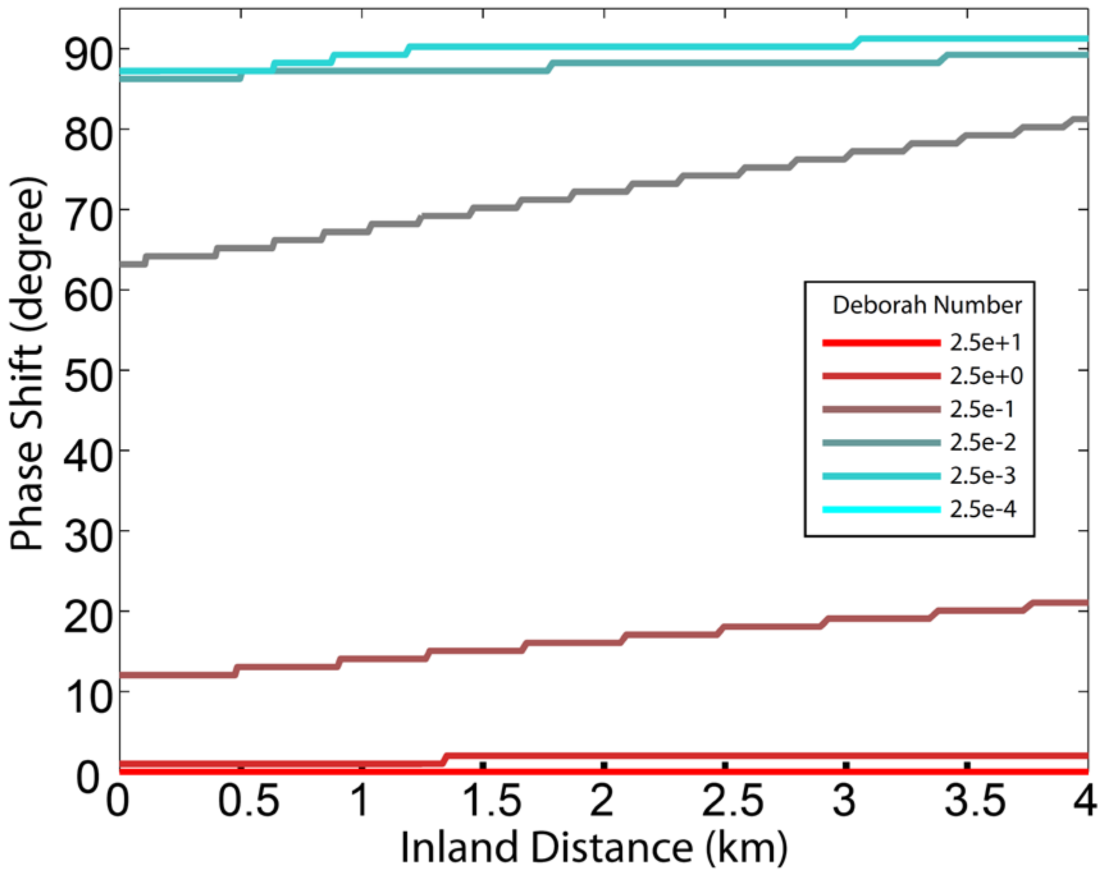

Figure 4.7: Distance dependence of the phase shift for laterally-locked models at a range of Deborah numbers. The redder colors represent more elastic models (higher *De*) while the bluer colors represent more viscous models (lower *De*).

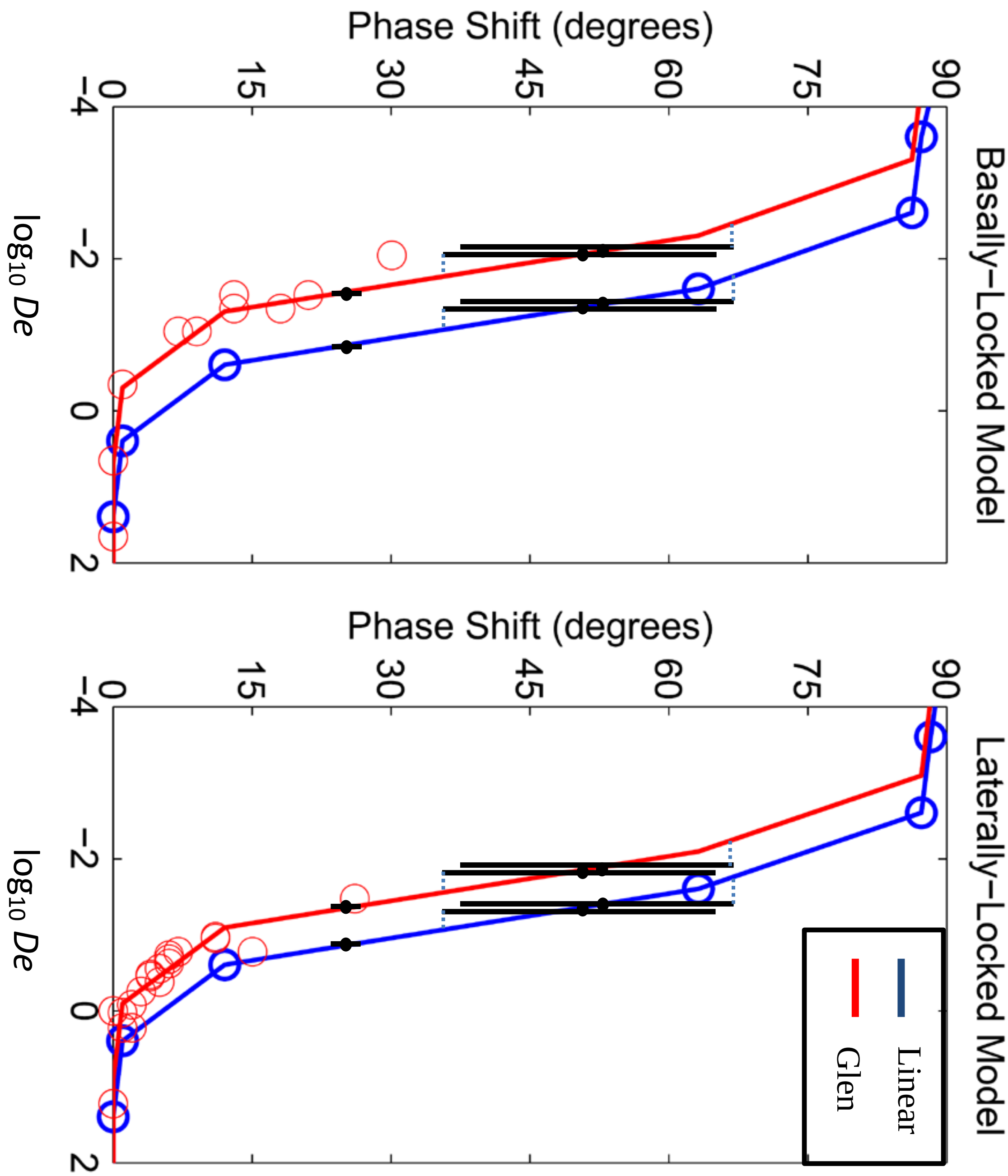

Figure 4.8: Fitting results for the data from Helheim Glacier (see section 4.3.3). The blue line is a linear fit, while the red line is an extrapolated version of the Glen flow fit. Finite element model results are shown as open circles. The data from Helheim Glacier are the solid black points, with error bars shown as the black lines. The values of the fit are tabulated in table 4.3.

	J_1	J_2	Relaxation Time	Retardation Time
Maxwell	$\frac{1}{\mu}$	$\frac{1}{\eta\omega}$	$\frac{\eta}{\mu}$	N/A
Kelvin	$\frac{\mu}{\mu^2 + (\eta\omega)^2}$	$\frac{\eta\omega}{\mu^2 + (\eta\omega)^2}$	N/A	$\frac{\eta}{\mu}$
Burgers	$\frac{1}{\mu_1} + \frac{\mu_2}{{\mu_2}^2 + (\eta_2\omega)^2}$	$\frac{1}{\eta_1\omega} + \frac{\eta_2\omega}{{\mu_2}^2 + (\eta_2\omega)^2}$	$\frac{p_1 \pm \sqrt{p_1 - 4p_2}}{2p_2}$	$\frac{\eta_2}{\mu_2}$

Table 4.1: Complex creep modulus real (J_1) and imaginary components (J_2), material relaxation and retardation time (where applicable) for a Maxwell, Kelvin, and Burgers model in one dimension. The placeholder variables used in the Burgers relaxation time correspond to: $p_1 = \left(\frac{\eta_1}{\mu_1} + \frac{\eta_2}{\mu_2}\right)$ and $p_2 = \left(\frac{\eta_1}{\mu_1}\frac{\eta_2}{\mu_2}\right)$.

		15°	30°	45°	60°	75°
	Semidiurnal	-0.23	-0.56	-0.80	-1.04	-1.37
$n = 1$	Diurnal	-0.23	-0.56	-0.80	-1.04	-1.37
	Fortnightly	-0.23	-0.56	-0.80	-1.04	-1.37
	Semidiurnal	-0.36	-0.69	-0.93	-1.17	-1.50
$n = 1.8$	Diurnal	-0.26	-0.59	-0.83	-1.07	-1.40
	Fortnightly	-0.26	-0.59	-0.83	-1.07	-1.40
	Semidiurnal	-0.50	-0.82	-1.07	-1.31	-1.64
$n = 3$	Diurnal	-0.32	-0.66	-0.90	-1.13	-1.47
	Fortnightly	-0.29	-0.63	-0.85	-1.09	-1.43
	Semidiurnal	-0.59	-0.92	-1.16	-1.40	-1.73
$n = 4$	Diurnal	-0.39	-0.72	-0.96	-1.20	-1.53
	Fortnightly	-0.29	-0.63	-0.87	-1.10	-1.44

Table 4.2: Logarithmic values of the Deborah number at a selection of phase shift values for the combined tidal solutions shown in figure 4.2D. Note that the phase shift behaves the same for the tidal forcing frequencies with a value of $n = 1$, and the value varies between the other solutions for nonlinear viscosity models.

	Linear Base	Glen Base	Linear Wall	Glen Wall
24	5.83	1.16	5.83	2.12
27	5.07	1.01	5.07	1.84
30	4.42	0.882	4.42	1.60
38	3.13	0.625	3.13	1.14
53	1.57	0.313	1.57	0.569
68	0.624	0.125	0.624	0.227
40	2.85	0.569	2.85	1.04
55	1.73	0.285	1.73	0.519
70	0.507	0.101	0.519	0.184

Table 4.3: Summary of the effective viscosities calculated for the Helheim Glacier using data from de Juan-Verger (2011). The columns correspond to the linear and Glen models for the basely-locked model (figure 3.8A) and the laterally-locked model (figure 3.8B). The data correspond to the data points from de Juan-Verger (2011) described in section 4.3.3 in bold, with the upper and lower error bars calculated as well. Each value is in terms of 10^{13} Pa · s.

	Ice Velocity	Tidal Interaction	Ice Shelf	Geometry	Basal Character	Thermal Profile
Bindschadler Ice Stream	300-800 m/yr	Continuous Motion	Yes	Wide and flat	Till	Poly.
Ekstrom Ice Shelf	250+ m/yr	None at 3 km inland	Yes	Narrow and flat	?	Poly.
Kamb Ice Stream	20-50 m/yr	Seismic evidence	Yes	Wide and flat	Till	Poly.
Pine Island Glacier	2 km/yr	None at 55 km inland	Yes	Narrow and flat	Till	Poly.
Thwaites Glacier	2 km/yr	?	Yes	Narrow and flat	Till	Poly.
Rutford Ice Stream	400-700 m/yr	Continuous Motion	Yes	Narrow and flat	Till	Poly.
Whillans Ice Plain	300-800 m/yr	Stick-slip	Yes	Wide and flat	Till	Poly.
Kangerdlussuaq	5 km/yr	?	Variable	Narrow and steep	Rock	Poly.
Helheim	8-11 km/yr	Continuous Motion	Variable	Narrow and steep	Rock	Poly.
Jakobshavn Isbrae	4-8 km/yr	?	Yes	Narrow and steep, tributary glaciers bend	Rock	Poly.
Columbia Glacier	2+ km/yr	Continuous Motion	No	Narrow and flat	Till	?
LeConte Glacier	4+ km/yr	Continuous Motion	No	Narrow and flat, with bend	Rock	?

Table 4.4: Summary of target glacier characteristics for a range of Antarctic, Greenland, and Alaskan glaciers. The columns show the ice velocity, the tidal behavior, the presence of an ice shelf, a brief summary of the geometry, the nature of the ice stream's bed, and

the temperature profile of the ice stream. For temperature, poly. refers to polythermal glaciers. References for most glaciers are summarized in chapter 1. References for Thwaites, Columbia, and LeConte glaciers are: Krimmel and Vaughn, 1987; Walters and Dunlap, 1987; Walters, 1989; Humphrey et al., 1993; Meier et al., 1994; O'neel et al., 2001; 2003; Rignot et al., 2002; Shepherd et al., 2002.

Appendix 4A: Spatial Distribution of Phase Shift

This appendix lists nine figures demonstrating the spatial distribution of the value of phase shift in the laterally-locked models. The first five figures (4A.1 to 4A.5) shows the phase shift for linear viscoelastic models at progressively smaller *De*. The other four figures show model results for the nonlinear viscoelastic models with the smallest *De* (and thus the largest spatial variability). Figures 4A.6 and 4A.7 show Glen model results, figure 4A.8 shows results for a Goldsby rheology with $n=1.8$, and figure 4A.9 shows phase shifts for a Goldsby rheology with $n=4$.

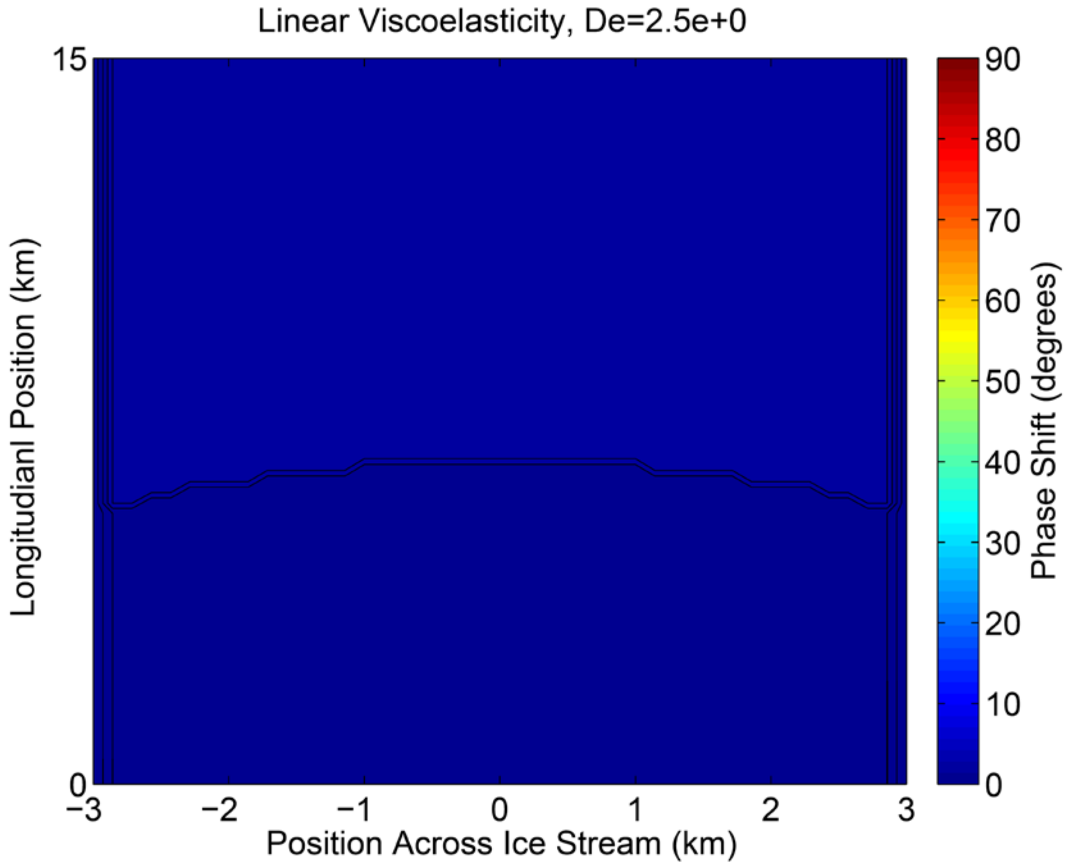

Figure 4A.1: Phase shift distribution for a linear viscoelastic model with *De* = 2.5e0 Pa · s.

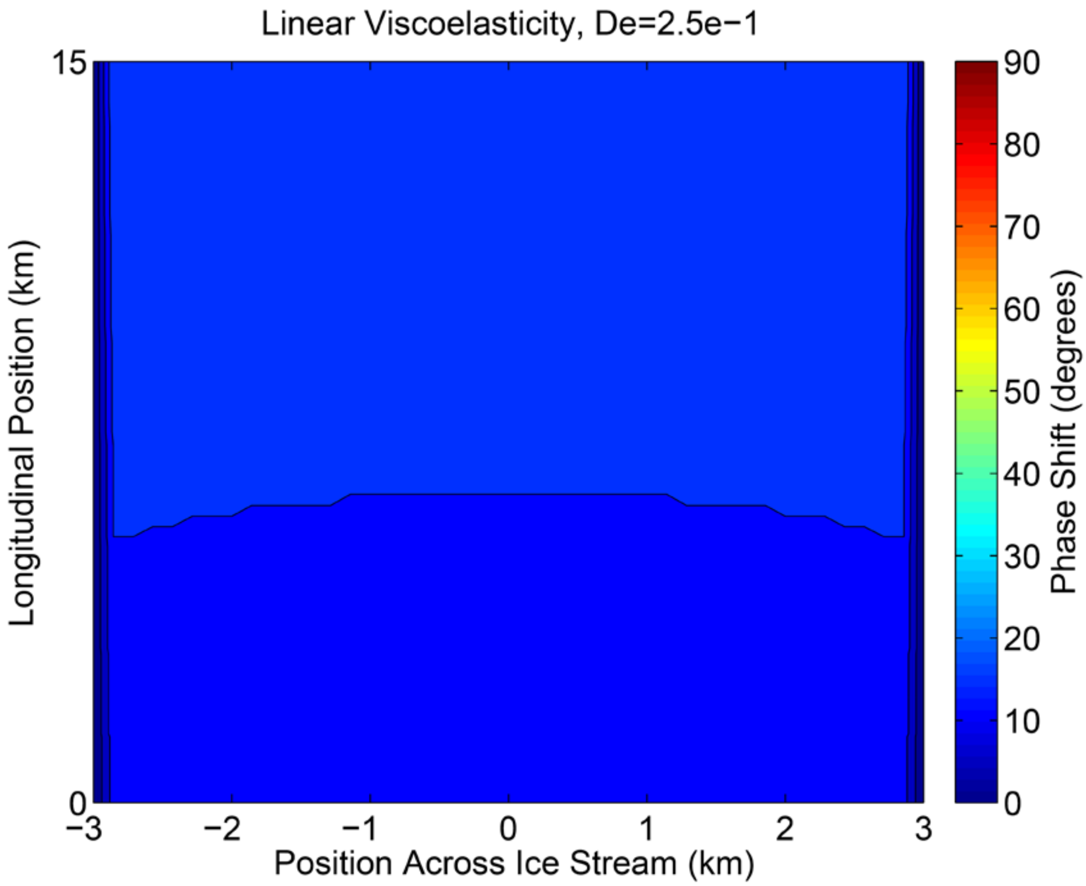

Figure 4A.2: Phase shift distribution for a linear viscoelastic model with *De* = 2.5e-1 Pa · s.

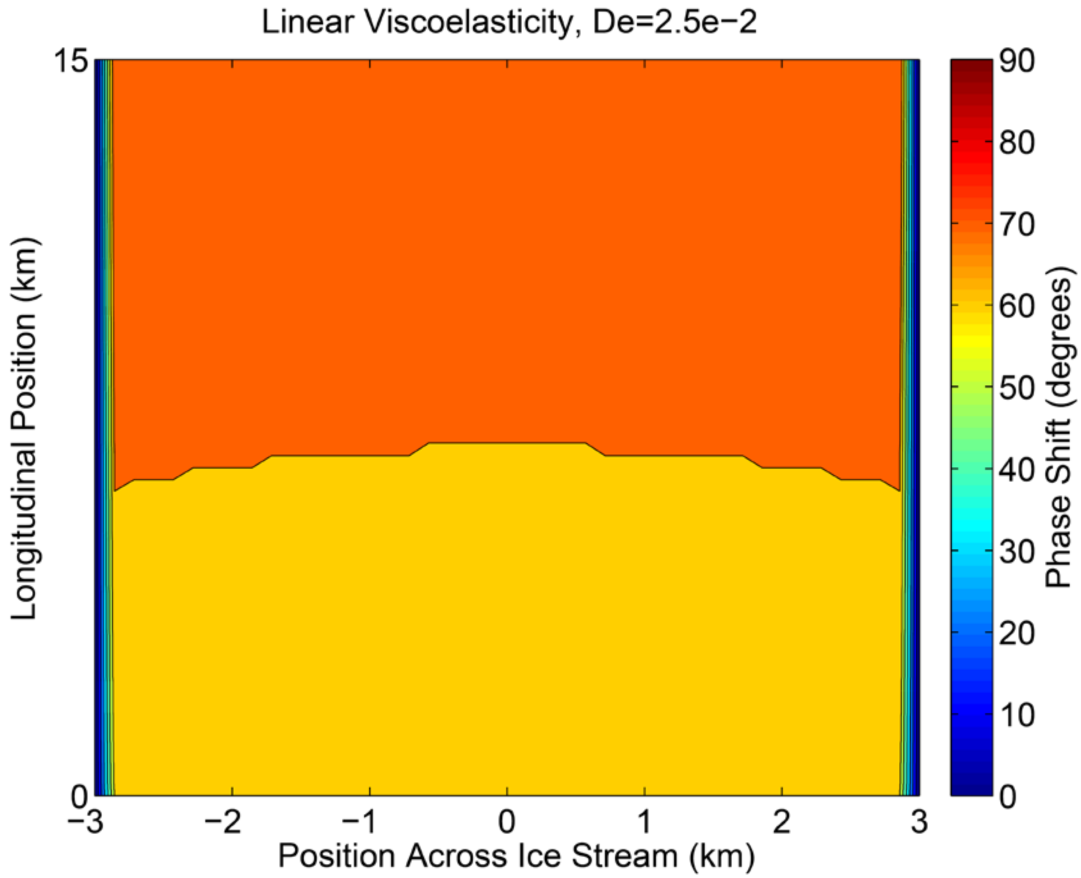

Figure 4A.3: Phase shift distribution for a linear viscoelastic model with *De* = 2.5e-2 Pa · s.

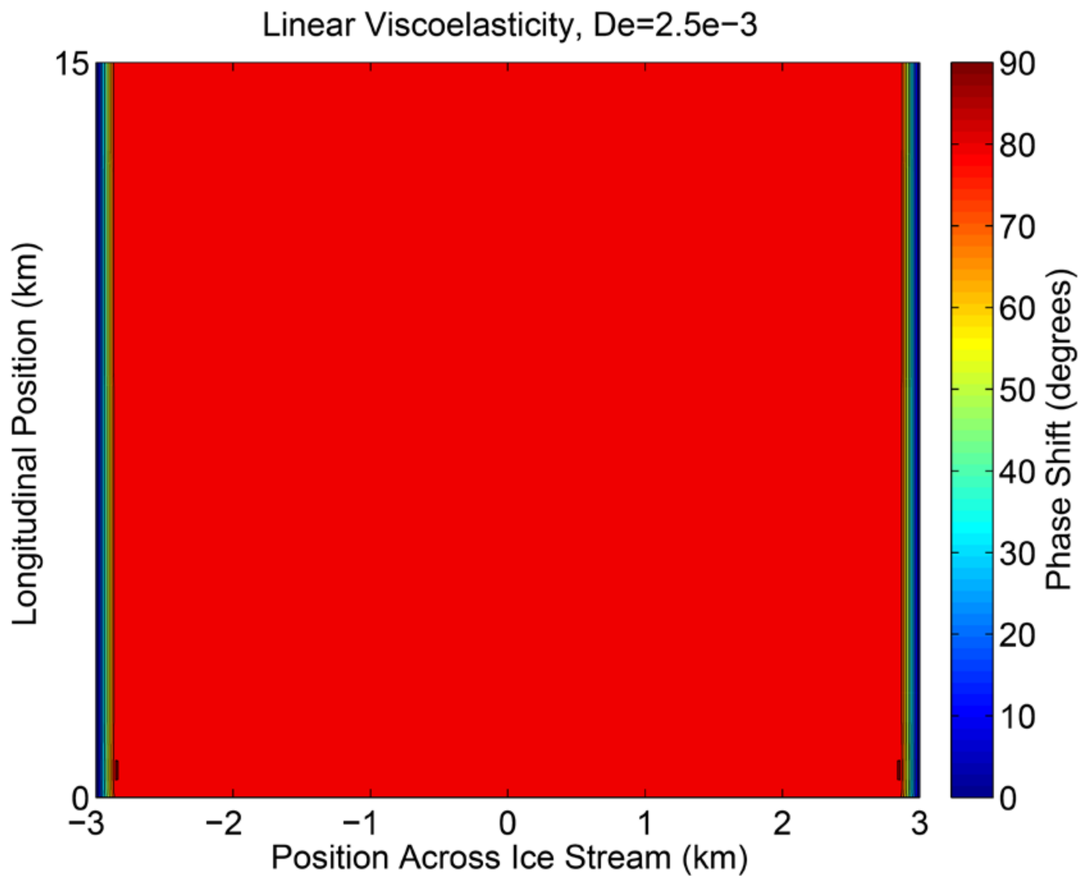

Figure 4A.4: Phase shift distribution for a linear viscoelastic model with *De* = 2.5e-3 Pa · s.

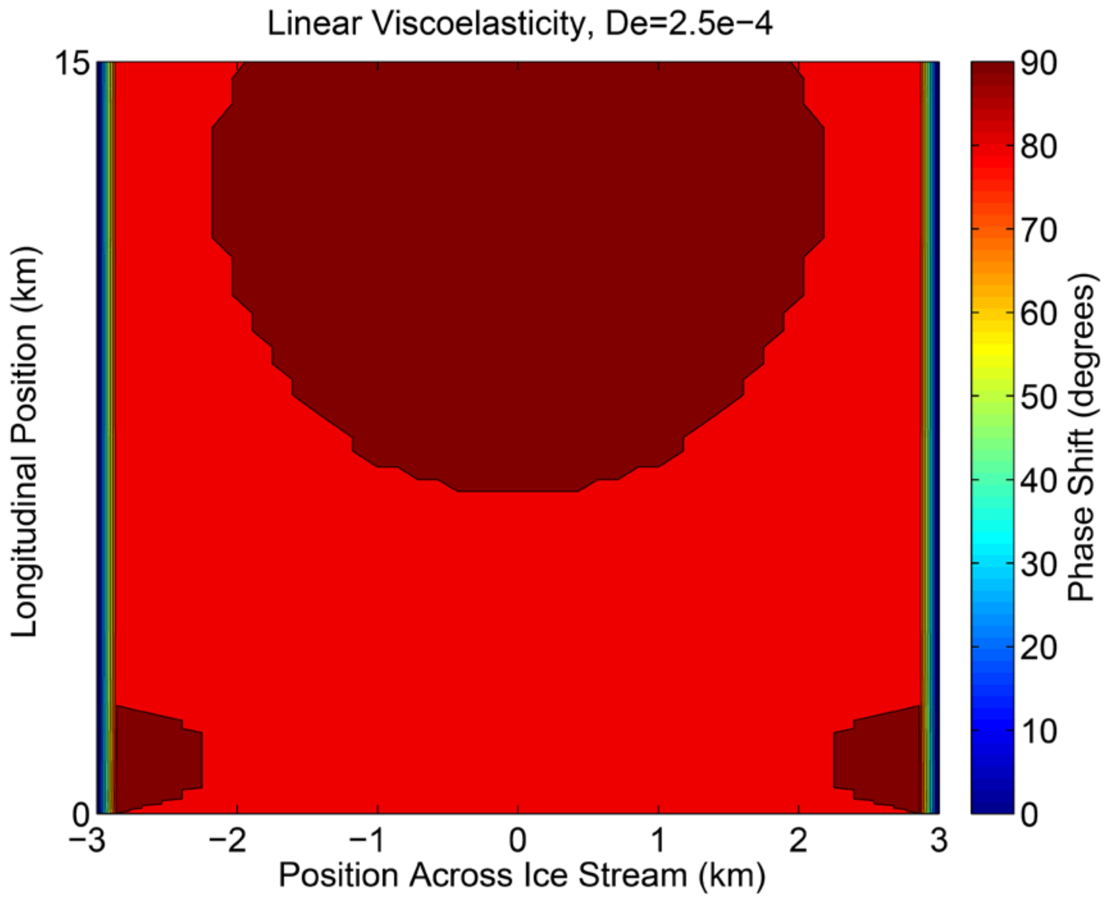

Figure 4A.5: Phase shift distribution for a linear viscoelastic model with *De* = 2.5e-4 Pa · s.

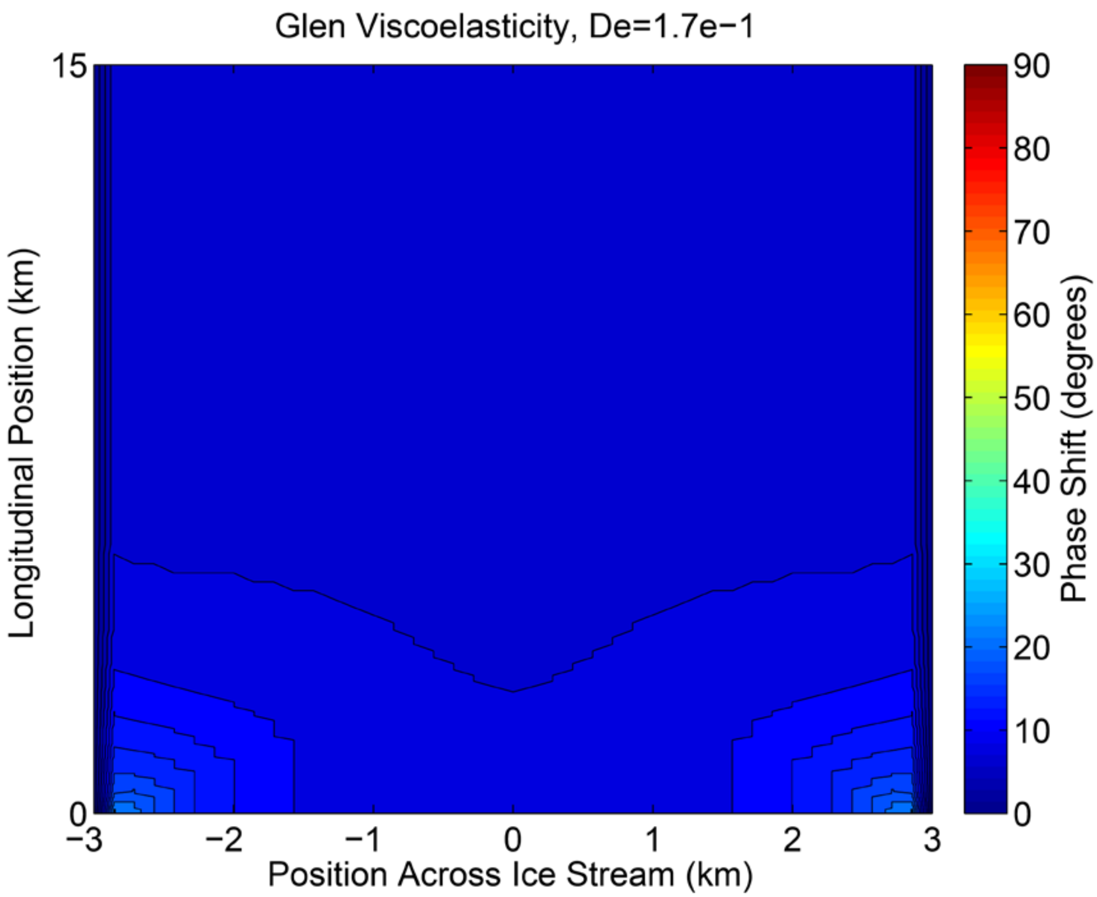

Figure 4A.6: Phase shift distribution for a Glen viscoelastic model (*n=3*) with *De* = 1.7e-1 Pa · s.

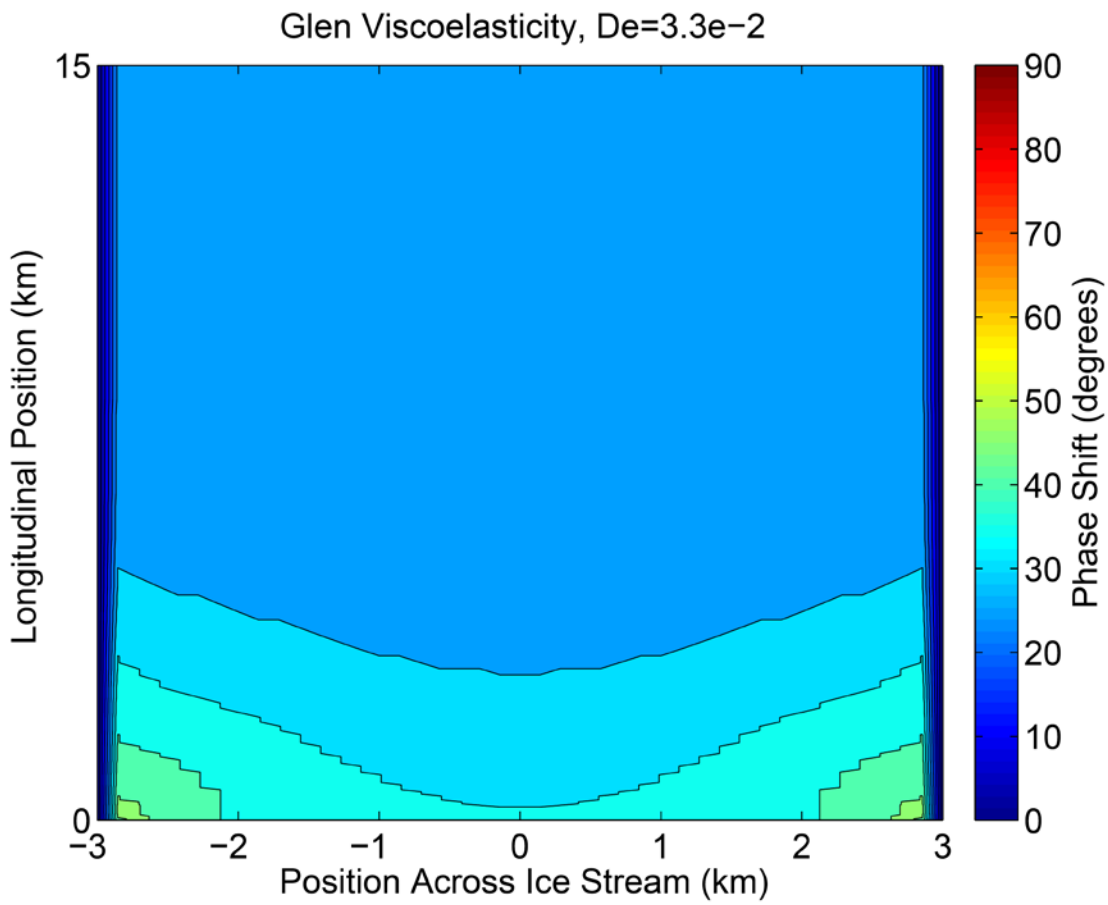

Figure 4A.7: Phase shift distribution for a Glen viscoelastic model (*n=3*) with *De* = 3.3e-2 Pa · s.

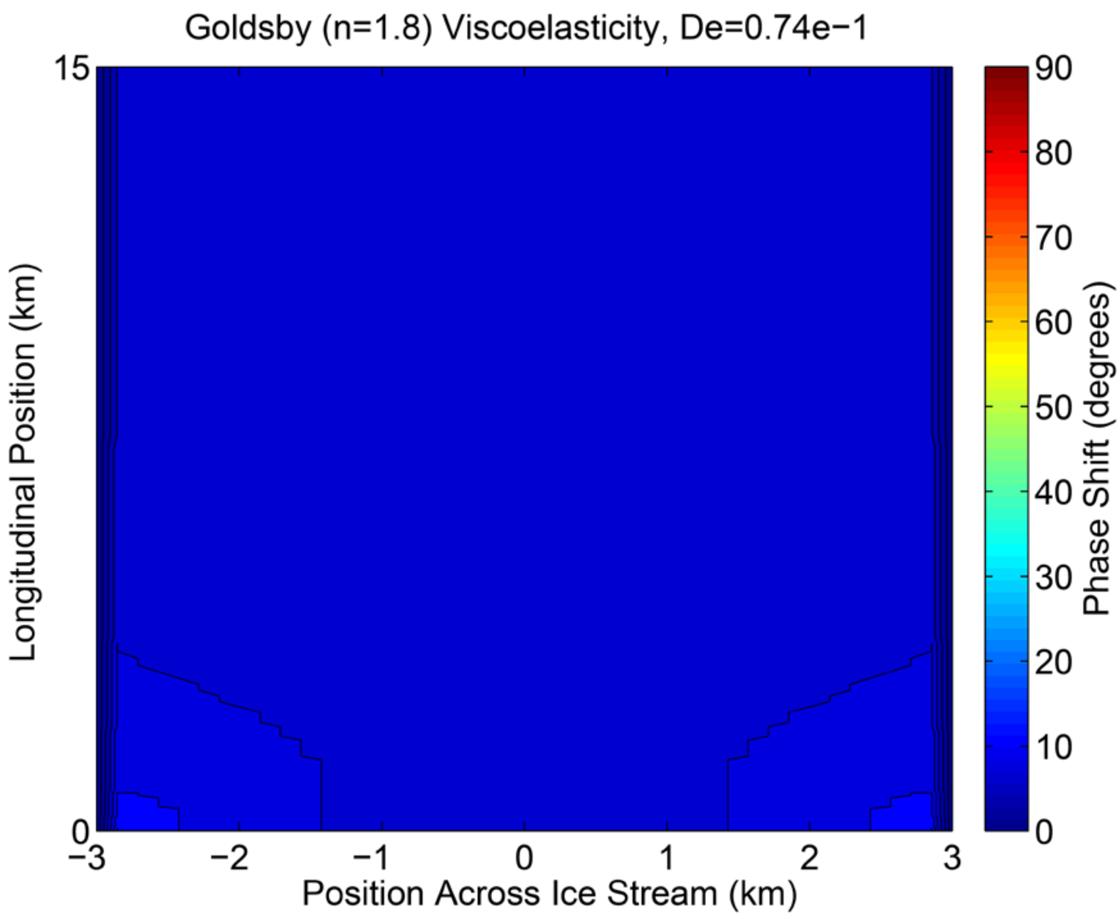

Figure 4A.8: Phase shift distribution for a Goldsby viscoelastic model (*n=1.8*) with *De* = 0.74e-1 Pa · s.

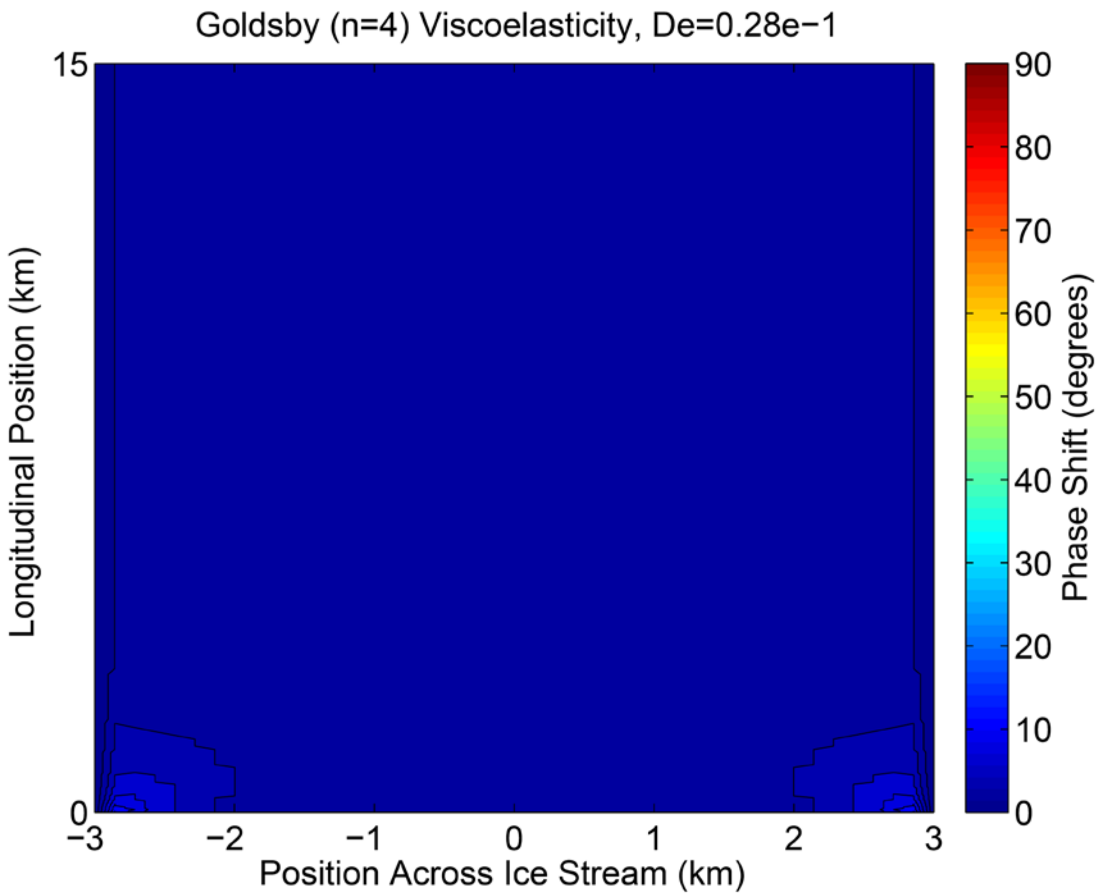

Figure 4A.9: Phase shift distribution for a Goldsby viscoelastic model (*n=4*) with *De* = 0.28e-1 Pa · s.